RAA 2016 Vol. **16** No. **2**, 26 (18pp) doi: 10.1088/1674–4527/16/2/026
http://www.raa-journal.org *http://iopscience.iop.org/raa*

Research in Astronomy and Astrophysics

Determining the type of orbits in the central regions of barred galaxies

Euaggelos E. Zotos and Nicolaos D. Caranicolas

Department of Physics, Section of Astrophysics, Astronomy and Mechanics, Aristotle University of Thessaloniki GR-541 24, Thessaloniki, Greece; *evzotos@physics.auth.gr*

Received 2015 April 17; accepted 2015 July 15

arXiv:1604.03376v1 [astro-ph.GA] 12 Apr 2016

Abstract We use a simple dynamical model which consists of a harmonic oscillator and a spherical component, in order to investigate the regular or chaotic character of orbits in a barred galaxy with a central spherically symmetric nucleus. Our aim is to explore how the basic parameters of the galactic system influence the nature of orbits, by computing in each case the percentage of chaotic orbits, as well as the percentages of different types of regular orbits. We also give emphasis to the types of regular orbits that support either the formation of nuclear rings or the barred structure of the galaxy. We provide evidence that the traditional x_1 orbital family does not always dominate in barred galaxy models since we found several other types of resonant orbits which can also support the barred structure. We also found that sparse enough nuclei, fast rotating bars and high energy models can support the galactic bars. On the other hand, weak bars, dense central nuclei, slowly rotating bars and low energy models favor the formation of nuclear rings. We also compare our results with previous related work.

Key words: galaxies: kinematics and dynamics

1 INTRODUCTION

It is well known to astronomers that axial symmetry in galaxies is only a first approximation. In essence, galaxies exhibit deviation from axial symmetry, which can be very small or more extended. In the latter category, we may include the case of barred galaxies. Observations indicate that a large percentage of disk galaxies, about 65%, show bar-like formations (e.g., Eskridge et al. 2000; Sheth et al. 2003). Observations also show that barred galaxies may display different characteristics. There are galaxies with a prominent barred structure and also galaxies with faint weak bars. Moreover, there are also barred galaxies with massive and less massive bulges. In some cases, the formation of the central bulges is the result caused by dynamical instabilities in the disk (Kormendy & Kennicutt 2004).

In fact, bars are non-axisymmetric structures that can redistribute the angular momentum of a galaxy, thus favoring the transport of gas through them to the inner regions where it may trigger star formation and play an important role in the evolution of these stellar systems (e.g., Muñoz-Tuñón et al. 2004; Sheth et al. 2005). In this way, considerable changes occur in the morphology and structure of barred galaxies. Such a change is exhibited by a significant increase in the mass of the bulge in galaxies with bars (e.g., Friedli & Martinet 1993; Marinova & Jogee 2007).

An important and striking phenomenon in barred galaxies is associated with nuclear rings, which are active sites of new star formation (e.g., Knapen et al. 1995; Mazzuca et al. 2008; Sandstrom et al. 2010; Hsieh et al. 2011). Some scientists have the impression that the formation of nuclear rings is due to the effect of the non axially symmetric potential of the bar in an area with plenty of interstellar gas. A key role in this mechanism is played by the torque of the bar, which causes the gas to form the nuclear rings (Kim et al. 2012b). Observations show that the rate of star formation in the nuclear rings is not only different in several types of barred galaxies but also varies significantly with time (e.g., Buta et al. 2000; Benedict et al. 2002; Comerón et al. 2010).

The formation and evolution of dust lanes and nuclear rings have been extensively studied using numerical simulations (e.g., Piner et al. 1995; Englmaier & Gerhard 1997; Maciejewski et al. 2002; Regan & Teuben 2003; Thakur et al. 2009). The formation of nuclear rings from the resonant interaction of gas with the potential of the bar appears not to be consistent with recent studies indicating that these formations are probably due to a different mechanism (e.g., Kim et al. 2012a). According to this mechanism, there is a centrifugal barrier which cannot be overcome by the inflowing gas. This barrier is responsible for the formation of the nuclear rings. Finally, recent research reveals that the more massive the bar is, the smaller the formed nuclear rings are. Here we should mention that the observational data justify the above results (Comerón et al. 2010).

Over recent decades, a huge amount of research work has been devoted to understanding the orbital structure in barred galaxy models (e.g., Athanassoula et al. 1983; Pfenniger 1984; Combes et al. 1990; Athanassoula 1992; Pfenniger 1996; Kaufmann & Contopoulos 1996; Olle & Pfenniger 1998; Pichardo et al. 2004). The reader can find more information about the dynamics of barred galaxies

in the reviews by Athanassoula (1984); Contopoulos & Grosbol (1989); Sellwood & Wilkinson (1993). We would like to point out that all the above-mentioned references on the dynamics of barred galaxies are exemplary rather than exhaustive. However, we should like to discuss briefly some of the recent papers on this subject. Skokos et al. (2002a) conducted an extensive investigation regarding the stability and morphology of both two-dimensional (2D) and three-dimensional (3D) periodic orbits in a fiducial model representative of a barred galaxy. The work was continued in the same vein in Skokos et al. (2002b), where the influence of the system's parameters on the 3D periodic orbits was revealed. Moreover, Kaufmann & Patsis (2005) presented evidence that in 2D models with sufficiently large bar axial ratios, stable orbits having propeller shapes play a dominant role in the bar structure. Manos & Athanassoula (2011) estimated the fraction of chaotic and regular orbits in both 2D and 3D potentials by computing several sets of initial conditions and studying how these fractions evolve when the energy and also basic parameters of the model, such as the mass, size and pattern speed of the bar, vary. Computing the statistical distributions of sums of position coordinates, Bountis et al. (2012) quantified weak and strong chaotic orbits in 2D and 3D barred galaxy models. A time-dependent barred galaxy model was utilized in Manos et al. (2013) in order to explore the interplay between chaotic and regular behavior of star orbits when the parameters of the model evolve. Finally, in Caranicolas & Papadopoulos (2007); Caranicolas & Zotos (2010), we conducted an investigation only regarding the issue of regular vs chaotic orbits in simple barred spiral potentials. In the present paper on the other hand, we shall try to contribute to this active field by classifying ordered orbits into different regular families and monitor how their rates evolve when basic quantities of the system vary.

Lees & Schwarzschild (1992), in a thorough pioneering study, analyzed the orbital content in the coordinate planes of triaxial potentials and also in the meridional plane of axially symmetric model potentials, focusing on regular families. Few years later, Carpintero & Aguilar (1998) developed a method based on the analysis of the Fourier spectrum of the orbits which can not only distinguish between regular and chaotic orbits, but also between loop, box and other resonant orbits either in 2D or 3D potentials. This spectral method was improved and applied in Muzzio et al. (2005) in order to identify the different kinds of regular orbits in a self-consistent triaxial model. The same code was improved even further in Zotos & Carpintero (2013), when the influence of the central nucleus and of the isolated integrals of motion (angular momentum and energy) on the percentages of orbits in the meridional plane of an axisymmetric galactic model composed of a disk and a spherical nucleus were investigated. In two recent papers, Caranicolas & Zotos (2013) and Zotos & Caranicolas (2013), analytical dynamical models describing the motion of stars in both disk and elliptical galaxies containing dark matter were used in order to investigate how the presence and the amount of dark matter influences the regular or chaotic nature of orbits as well as the behavior of the different families of resonant orbits.

Taking into account all the above, there is no doubt that knowing the overall orbital structure in the central regions of barred galaxies is an issue of paramount importance. For this reason, we decided to use a simple model that describes local motion near the central area of a barred galaxy. Our aim is to investigate the regular or chaotic character of motion and to study how the different families of orbits are affected by varying the physical quantities entering the model. Here we must point out that the present article belongs to a series of papers (Zotos & Carpintero 2013; Caranicolas & Zotos 2013; Zotos & Caranicolas 2013; Zotos & Caranicolas 2014) that have as their main objective the orbit classification (not only regular versus chaotic but also separating regular orbits into different regular families) in different galactic gravitational potentials. Thus, we decided to follow a similar structure and apply the same numerical approach to all of them.

The structure of the present paper is as follows: In Section 2 we present a detailed description of the properties of our gravitational galactic model. All the different computational methods used in order to determine the character of orbits are described in Section 3. In the following, Section 4, we explore how the basic parameters involved in the dynamical system influence the percentages of all types of orbits and which of them support either a bar or ring structure. Our article ends with Section 5, where the conclusions and the discussions of this research are presented.

2 PROPERTIES OF THE GALACTIC MODEL

The total gravitational potential $\Phi(x, y)$ consists of two components: the bar potential $\Phi_{\rm b}$ and the central, spherical component $\Phi_{\rm n}$. For the description of properties of the bar we use the following simple harmonic oscillator potential

$$\Phi_{\rm b}(x, y) = \frac{\omega^2}{2}\left(x^2 + \alpha y^2\right), \tag{1}$$

where α is a parameter corresponding to the strength of the bar, while the parameter ω is used for consistency of the galactic units.

The spherically symmetric nucleus is modeled by a Plummer potential (e.g., Binney & Tremaine 2008)

$$\Phi_{\rm n}(x, y) = \frac{-GM_{\rm n}}{\sqrt{x^2 + y^2 + c_{\rm n}^2}}. \tag{2}$$

Here G is the gravitational constant, while $M_{\rm n}$ and $c_{\rm n}$ are the mass and the scale length of the nucleus, respectively. This potential has been used successfully in the past in order to model and therefore interpret the effects of the central mass component in a galaxy (see, e.g. Hasan & Norman 1990; Hasan et al. 1993; Zotos 2012a; Zotos & Carpintero 2013). At this point, we must make clear

that Equation (2) is neither intended to represent the potential of a black hole nor that of any other compact object, but just the potential of a dense and massive nucleus. Therefore, any relativistic effects are out of the scope of this work.

The 2D $\Phi(x,y)$ was chosen because we believe that it is an approximation for describing local motion near the central parts of a barred galaxy. Our choice was motivated by two reasons: (i) the small number of input parameters of Equation (1) is an advantage concerning the performance and speed of the numerical calculations in comparison with other much more complicated potentials describing bars (i.e. the Ferrers bar, Ferrers 1877) and (ii) it corresponds to a constant density profile which, however, can be assumed when studying local motion very close to the galactic center, like in our case. Furthermore, the same potential has been used successfully in many previous works for modeling the properties of local motion in the central parts of a galaxy (e.g., Caranicolas 1998; Caranicolas & Karanis 1998; Caranicolas & Papadopoulos 2005; Zotos 2011, 2012b). Note that the density corresponding to the total potential $\Phi(x,y)$, on the other hand, is not constant but it declines with increasing distance from the origin due to the contribution of the spherical nucleus.

The bar rotates counterclockwise at a constant angular velocity $\Omega_{\rm b}$. Therefore the effective potential is

$$\Phi_{\rm eff}(x,y) = \Phi(x,y) - \frac{1}{2}\Omega_{\rm b}^2\left(x^2+y^2\right). \qquad (3)$$

In our study, we use the well-known system of galactic units, where the unit of length is 1 kpc, the unit of mass is $2.325\times10^7 {\rm M}_\odot$ and the unit of time is 0.9778×10^8 yr. The velocity unit is 10 km s^{-1}, the unit of angular momentum (per unit mass) is 10 km kpc^{-1} s^{-1}, while G is equal to unity. The energy unit (per unit mass) is 100 km^{2}s^{-2}. In these units, the values of the involved parameters are: $\omega=10$, $\alpha=4$, $M_n=50$ (corresponding to 1.2×10^9 $M_\odot$), $c_{\rm n}=0.25$ and $\Omega_{\rm b}=1$. This set of the values of the parameters defines the Standard Model (SM).

The equations of motion are described by

$$\ddot{\boldsymbol{r}} = -\boldsymbol{\nabla}\Phi_{\rm eff} - 2\left(\boldsymbol{\Omega_{\rm b}}\times\dot{\boldsymbol{r}}\right), \qquad (4)$$

where the term $-2\left(\boldsymbol{\Omega_{\rm b}}\times\dot{\boldsymbol{r}}\right)$ represents the Coriolis force. Decomposing Equation (4) into its x and y parts, we obtain

$$\ddot{x} = -\frac{\partial\Phi_{\rm eff}}{\partial x} + 2\Omega_{\rm b}\dot{y}, \quad \ddot{y} = -\frac{\partial\Phi_{\rm eff}}{\partial y} - 2\Omega_{\rm b}\dot{x}, \qquad (5)$$

where the dot indicates derivative with respect to time.

In the same vein, the equations describing the evolution of a deviation vector $\boldsymbol{w} = (\delta x, \delta y, \delta\dot{x}, \delta\dot{y})$ which joins the corresponding phase space points of two initially nearby orbits, needed for the calculation of standard chaos indicators (SALI in our case), are given by the following variational equations

$$\begin{aligned}
(\dot{\delta x}) &= \delta\dot{x}, \quad (\dot{\delta y}) = \delta\dot{y},\\
(\dot{\delta\dot{x}}) &= -\frac{\partial^2\Phi_{\rm eff}}{\partial x^2}\delta x - \frac{\partial^2\Phi_{\rm eff}}{\partial x\partial y}\delta y + 2\Omega_{\rm b}\delta\dot{y},\\
(\dot{\delta\dot{y}}) &= -\frac{\partial^2\Phi_{\rm eff}}{\partial y\partial x}\delta x - \frac{\partial^2\Phi_{\rm eff}}{\partial y^2}\delta y - 2\Omega_{\rm b}\delta\dot{x}. \qquad (6)
\end{aligned}$$

Consequently, the corresponding Hamiltonian to the effective potential given in Equation (3) reads

$$H_{\rm J} = \frac{1}{2}\left(\dot{x}^2+\dot{y}^2\right) + \Phi_{\rm eff}(x,y) = E_{\rm J}, \qquad (7)$$

where $\dot{x}$ and $\dot{y}$ are momenta per unit mass, conjugate to x and y respectively, while $E_{\rm J}$ is the numerical value of the Jacobi integral, which is conserved. Thus, an orbit with a given value for its Jacobi integral is restricted in its motion to regions in which $E_{\rm J}\leq\Phi_{\rm eff}$, while all other regions are forbidden with respect to the star.

3 COMPUTATIONAL METHODS

For distinguishing between order and chaos in our models we use the SALI method (Skokos 2001) (for more details on how the SALI method works see Zotos & Carpintero 2013). We chose, for each value of the free parameter of the potential, a dense grid of initial conditions in the $(x,\dot{x})$ phase plane, regularly distributed in the area allowed by the value of the energy $E_{\rm J}$. In all cases, $y_0=0$, while $\dot{y_0}$ is found from the Jacobi integral (Eq. (7)). The distance between the points of the gird along the x and $\dot{x}$ directions, or in other words its density, was calibrated in such a way so that every grid contains around 15 000 orbits. For each initial condition, we integrated the equations of motion (5) as well as the variational equations (6) with a double precision Bulirsch-Stoer algorithm (e.g., Press et al. 1992). In all cases, the value of the Jacobi integral (Eq. (7)) was conserved better than one part in 10^{-11}, although for most orbits, it was better than one part in 10^{-12}.

All initial conditions of orbits are numerically integrated for 10^4 time units which correspond to about 10^{12} yr or in other words to about 100 Hubble times. This vast time of numerical integration is justified due to the presence of the so called "sticky orbits"[1]. Therefore, if the integration time is too short, any chaos indicator will misclassify sticky orbits as regular ones (see Appendix A for more details and examples). In our work we decided to integrate all orbits for a time interval of 10^4 time units in order to correctly classify sticky orbits with sticky periods of at least 100 Hubble times. At this point, it should be clarified that sticky orbits with sticky periods larger than 10^4 time units will be counted as regular ones, since such extremely high sticky periods are completely out of the scope of our research.

The distinction between order and chaos is only a first step for interpreting the overall orbital structure of the

[1] A sticky orbit is a chaotic orbit which behaves as a regular one for a long time period before revealing its true chaotic nature.

galactic system. The second and more important step is the classification of ordered orbits into different regular families. For this purpose we use the frequency analysis of Carpintero & Aguilar (1998) for categorizing regular orbits. About thirty years ago, Binney & Spergel (1982, 1984) proposed a computational method, dubbed "spectral dynamics" for the task of orbit classification, while later on Šidlichovský & Nesvorný (1996) and Carpintero & Aguilar (1998) substantially improved this method. Zotos & Carpintero (2013) further refined the numerical code for classifying orbits in the meridional (R, z) plane. The very same algorithm was used in all the papers of this series: Zotos & Carpintero (2013); Caranicolas & Zotos (2013); Zotos & Caranicolas (2013); Zotos & Caranicolas (2014), as well as in Muzzio et al. (2005) and Carpintero & Muzzio (2012).

4 NUMERICAL RESULTS

In this section, we shall present all the numerical results of our research. We numerically integrate several sets of orbits in order to distinguish between regular and chaotic motion. We use the initial conditions of orbits mentioned in Section 3 in order to construct the corresponding grids, always taking values inside the Zero Velocity Curve (ZVC) defined by

$$\frac{1}{2}\dot{x}^2 + \Phi_{\rm eff}(x, y = 0) = E_{\rm J}. \tag{8}$$

In most cases, the value of the Jacobi integral was set to $E_{\rm J} = 1.5$ and kept constant. However in the last subsection where we investigate the influence of the orbital energy, the value of the Jacobi integral is variable. We chose an energy level which gives $x_{\max} \simeq 1$ kpc, where $x_{\max}$ is the maximum possible value of the coordinate x on the $(x, \dot{x})$ phase plane, since our study is focused on local motion of stars. Once the values of the parameters are chosen, we compute a set of initial conditions as described in Section 3 and integrate the corresponding orbits calculating the value of SALI and then classifying the regular orbits into different families. Each grid contains roughly a total of 15 000 initial conditions $(x_0, \dot{x_0})$ of orbits with $y_0 = 0$, while $\dot{y_0}$ is always obtained from the Jacobi integral (Eq. (7)). In each case, we only let one parameter vary, while all the others have values according to the SM described in Section 2.

The numerical calculations show that in our barred galaxy model there are seven main types of orbits: (i) box orbits; (ii) 1:1 resonant orbits; (iii) 1:2 resonant orbits (type a); (iv) 1:2 resonant orbits (type b); (v) 2:3 resonant orbits; (vi) 3:4 resonant orbits, and (vii) chaotic orbits. Apart from the main families of orbits, however, several secondary resonances are also present.

In Figure 1(a)–(f) we present an example of each of the six basic types of regular orbits, while Figure 2(a)–(f) shows characteristic examples of the secondary resonant orbits. The box orbit shown in Figure 1(a) was computed until $t = 50$ time units, while all the parent[2] periodic orbits were computed until one period was completed. The black thick curve circumscribing each orbit is the limiting curve in the (x, y) plane defined as $\Phi_{\rm eff}(x, y) = E_{\rm J}$.

In Table 1 we provide the type, the initial conditions and the values of the variable parameters for all the depicted orbits. In the resonant cases, the initial conditions and the period $T_{\rm per}$ correspond to the parent periodic orbits. Here we would like to point out that resonant 1:2 type b orbits and resonant 1:3 orbits are only present in galaxy models with relatively high orbital energy $(E_{\rm J} > 100)$.

At this point, we would like to clarify some issues regarding the nomenclature of the orbits in our model. In earlier related articles, orbits in barred galaxies are usually classified into four main categories: the x_1 family which consists of elongated orbits along the bar, families x_2 and x_3 the orbits of which are also elongated but perpendicular to the bar and the retrograde x_4 family (e.g., Contopoulos & Papayannopoulos 1980). In the present case however, we decided to follow for consistency the same classification used in all previous papers of this series, according to which the orbits are separated into three main categories: (i) box orbits, (ii) $n : m$ resonant orbits, and (iii) chaotic orbits. According to our notation, all resonant orbits have the following recognizable $n : m$ oscillatory pattern: a resonant orbit completes m oscillations perpendicular to the major axis of the bar in the time that it takes the orbit to perform n circuits along the major axis. Furthermore, an $n : m$ resonant orbit would be represented by m distinct islands of invariant curves in the $(x, \dot{x})$ phase plane and n distinct islands of invariant curves in the $(y, \dot{y})$ surface of section. In our research, we searched for resonant orbits $n : m$ up to $n, m \leq 9$; therefore, for all higher resonant orbits the numerical code assigns "box" classification (this is a usual technique in orbit classification), which is correct for $n \neq m$ (high resonant box orbits, e.g., Caranicolas & Barbanis 1982). As was pointed out in the review of Sellwood & Wilkinson (1993) (p. 31), there are several different notations regarding the naming of the orbital families in barred galaxies. Traditionally, orbits are named $m : l$, where m denotes the number of radial oscillations an orbit performs before it closes, while l corresponds to the number of turns of the orbit around the center of the potential. Throughout the paper, we shall use the first notation which, from our point of view, is more descriptive and better fits our computational procedures.

It is of particular interest to determine which types of regular orbits support the barred structure in our galactic model. Looking carefully at the main types of orbits shown in Figure 1(a)–(f) it can be seen that the box and the 1:2 (types a and b) resonant orbits are the ones we are looking for. We also observe in Figure 2(a)–(f) that, apart from the 7:9 resonant family, all the other secondary resonances

[2] For every orbital family there is a parent (or mother) periodic orbit, that is, an orbit that describes a closed figure. Perturbing the initial conditions which define the exact position of a periodic orbit we generate quasi-periodic orbits that belong to the same orbital family and librate around their closed parent periodic orbit.

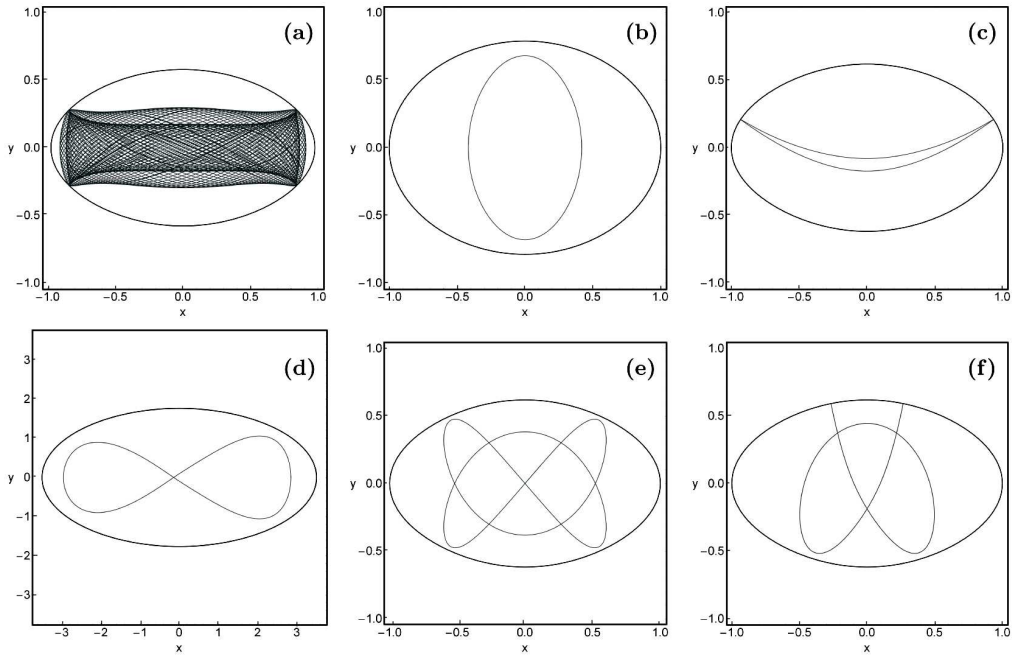

Fig. 1 Collection of the six basic types of orbits in our barred galaxy model: (a) box orbit; (b) 1:1 resonant orbit; (c) 1:2 resonant type a; (d) 1:2 resonant type b (figure-eight); (e) 2:3 resonant type; (f) 3:4 resonant orbit.

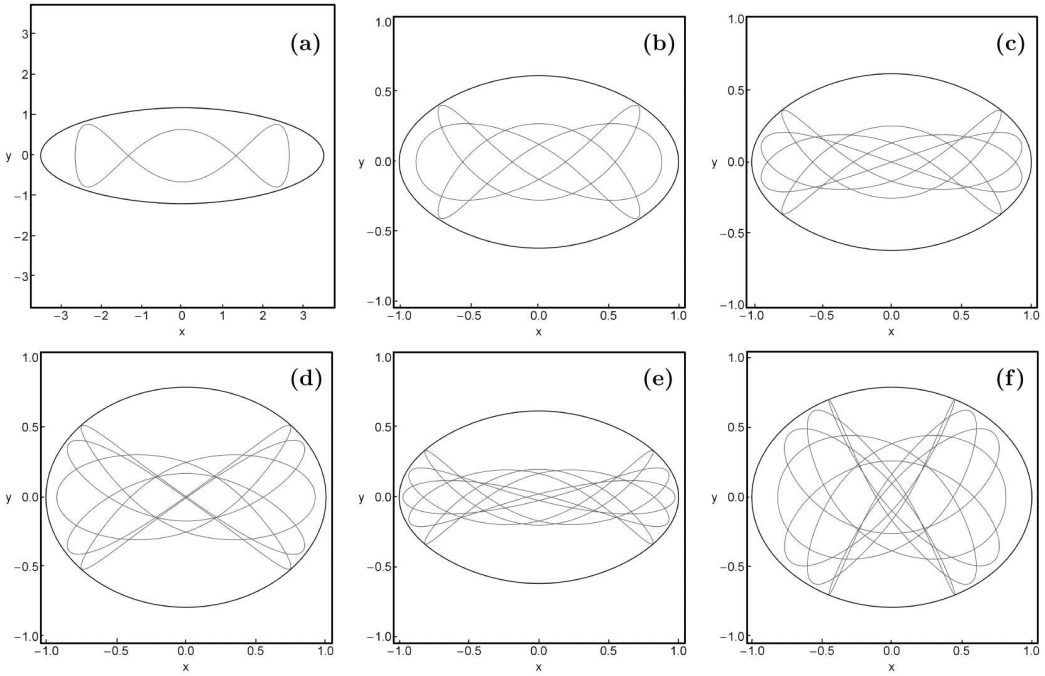

Fig. 2 Characteristic examples of six secondary resonant orbits in our barred galaxy model: (a) 1:3 resonant orbit; (b) 3:5 resonant orbit; (c) 4:7 resonant type; (d) 5:7 resonant type; (e) 5:9 resonant orbit; (f) 7:9 resonant orbit.

may support, more or less, the barred structure. In order to quantify our search for orbits supporting the bar, we must define a mathematical criterion thus distinguishing which types of orbits have the ability to support the bar. This issue can be solved if we exploit the geometry of the orbits. In particular, we compute the maximum values of the x and y coordinates of the regular orbits, $x_{\max}$ and $y_{\max}$ respectively, along the numerical integration. Then, the ratio $g = x_{\max}/y_{\max}$ defines whether an orbit supports the barred structure or not. The threshold value regarding the

Table 1 Type, model and initial conditions of the orbits shown in Figs. 1(a)–(f) and 2(a)–(f). In all cases, $y_0 = 0$ and $\dot{y_0}$ is found from the Jacobi integral, while $T_{\rm per}$ is the period of the resonant parent periodic orbits.

Figure	Type	α	$c_{\rm n}$	$\Omega_{\rm b}$	$E_{\rm J}$	x_0	$\dot{x_0}$	$T_{\rm per}$
1a	box	4	0.50	1.0	1.5	–0.91000000	0.00000000	–
1b	1:1	2	0.25	1.0	1.5	0.41867323	0.00000000	0.33573521
1c	1:2 (type a)	4	0.25	1.0	1.5	0.60531937	9.66513936	0.44222096
1d	1:2 (type b)	4	0.25	1.0	593	2.84610131	0.00000000	0.61819761
1e	2:3	4	0.25	0.0	1.5	0.00000000	13.08286668	0.73057544
1f	3:4	4	0.25	0.0	1.5	0.09738430	7.70724765	0.96330681
2a	1:3	9	0.25	1.0	593	2.64862858	0.00000000	0.61518671
2b	3:5	4	0.25	0.5	1.5	0.88078044	0.00000000	1.21951427
2c	4:7	4	0.25	0.5	1.5	0.00000000	18.96771378	1.69575428
2d	5:7	2	0.25	1.0	1.5	0.92613552	0.00000000	2.19852734
2e	5:9	4	0.25	0.5	1.5	–0.97466418	0.00000000	2.16072089
2f	7:9	2	0.25	1.0	1.5	0.81782083	0.00000000	2.86034493

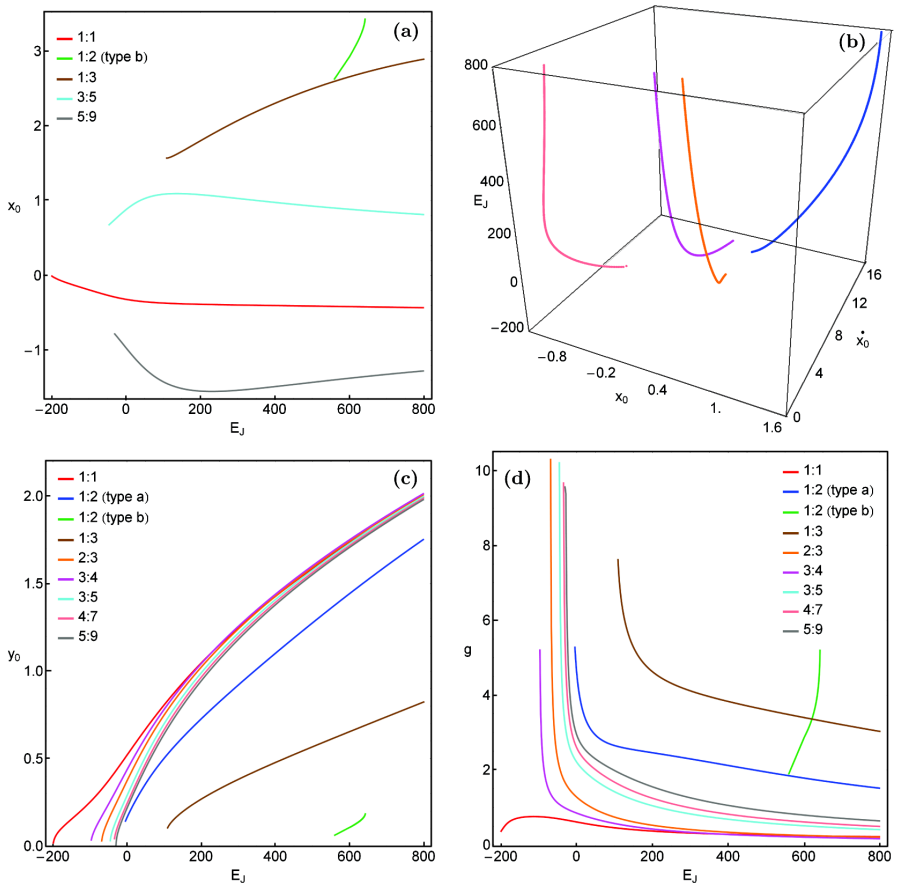

Fig. 3 (a-*upper left*): The $(x, E_{\rm J})$ and (b-*upper right*): the $(x, \dot{x}, E_{\rm J})$ characteristic curves of the orbital families for SM; (c-*lower left*): The $(y, E_{\rm J})$ characteristic diagram for all the orbital families; (d-*lower right*): A $(g, E_{\rm J})$ diagram showing which types of resonant families support the galactic bar. The color code is the same in all panels.

ratio strongly depends on the strength of the bar. Our numerical calculations suggest that a safe threshold for the ratio is the value $\sqrt{\alpha}$. Therefore, all types of regular orbits with values $g \geq \sqrt{\alpha}$ can support the barred structure.

One of the most interesting structures that are often observed in barred galaxies are rings. There are three main types: (i) nuclear rings situated near the central nucleus, (ii) inner rings surrounding the bar and (iii) outer rings with a relatively extended diameter. In this work, we investigate

the orbital properties near the central region of the barred galaxy and therefore, we only focus our study on nuclear rings. Bars have a natural tendency to concentrate gas near the nucleus but also can setup resonances which usually act as focal points for the gas flow. The reader can find more details about rings in barred galaxies in the review of Knapen (2004). We argue that 1:1 resonant orbits with approximately $0.5 < g < 1.5$ (both prograde and retrograde) are the best candidates for supporting the nuclear ring structure in barred galaxies. Thus, we shall pay special attention to how the basic parameters of the system affect the amount of 1:1 resonant orbits.

In Figure 3(a), we present a very informative diagram, the so-called "characteristic" orbital diagram (Contopoulos & Mertzanides 1977; Contopoulos & Barbanis 1985; Contopoulos & Magnenat 1985) for SM (except the 1:3 resonance for which $\alpha = 9$). It shows the evolution of the x coordinate of the initial conditions of the parent periodic orbits of each orbital family as a function of their orbital energy $E_{\rm J}$ (Jacobi constant). Here we should emphasize that for orbits starting perpendicular to the x-axis, we only need the initial condition of x_0 in order to locate them on the characteristic diagram. On the other hand, for orbits not starting perpendicular to the x-axis (i.e., the 1:2 type a, 2:3, 3:4 and 4:7 families) initial conditions like position-velocity pairs $(x, \dot{x})$ are required and, therefore, the characteristic diagram is now 3D, providing full information regarding the interrelations of the initial conditions in a tree of families of periodic orbits (Fig. 3(b)). Furthermore, the diagram shown in Figure 3(c) is another type of "characteristic" diagram (Sellwood & Wilkinson 1993; Binney & Tremaine 2008; Zotos 2013), where the value of the Jacobi integral E_J is plotted against the coordinate where the minor axis of the bar crosses the y-axis. As can be seen in Figures 1 and 2, all the higher resonant orbits encountered in our potential (i.e., the 2:3, 3:4, 3:5, 4:7 and 5:9 resonant orbits) have complicated shapes thus crossing the y-axis multiple times and at several positions. When constructing the diagram shown in Figure 3(c), we considered where all these higher resonant orbits crossed with higher absolute values of y_0.

In the same vein, we decided to create a new type of diagram which is called the "support diagram" and it is presented in Figure 3(d). In this diagram, we see the evolution of the g parameter of the parent periodic orbits for each family as a function of the energy $E_{\rm J}$ for SM. The aim of this plot is to help us decide which types of resonant orbits support the bar and which do not. The diagram works as follows: the higher a curve is (in other words, greater values of g) corresponding to a particular resonant family, the more supportive the barred structure is for this orbital family. We observe that both types of the 1:2 family as well as the 1:3 family highly support the bar, while on the other hand the 1:1 family has no contribution whatsoever to the bar (this family favors nuclear ring formation). Here we should note that the 1:2 type b family bifurcates from the main 1:2 type a family and it is only present at relatively high energy levels ($561 < E_{\rm J} < 642$). Moreover, we may say that in general terms higher resonant orbits such as the 3:5, 4:7 and 5:9 families can also support the bar, but the 2:3 and 3:4 resonant families can only support it at low energies.

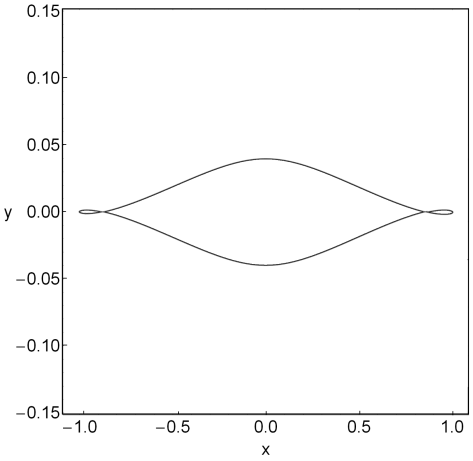

Fig. 4 A highly unstable x_1 periodic orbit in SM. The initial conditions and more details are given in the text.

It is widely accepted that galactic bars are in fact created by regular orbits which circulate around the so-called "x_1" periodic orbits (e.g., Skokos et al. 2002a,b) The x_1 orbits are elongated along the bar's major axis and usually have the shape of simple ellipses. However, with increasing energy, they can form a cusp and even two loops at the extremities.

In Figure 4, we present a highly unstable (Stability Index (S.I.) $= -17.24$) x_1 periodic orbit in SM with initial conditions: $x_0 = 0.86508078$, $y_0 = 0$, $\dot{x_0} = 6.31880018$, while the value of $\dot{y_0}$ was obtained from the Jacobi integral. Our numerical calculations indicate that, over the entire range of $E_{\rm J}$, our galactic model does not support the x_1 orbital family. This is true because the position of the parent periodic orbit in the $(x, \dot{x})$ phase plane is deeply buried in the chaotic region (see Fig. 5(c)) without any indication of an existing stability island around the periodic point which could support x_1 quasi-periodic orbits. Moreover, our computations reveal that in our barred galaxy model the x_1 periodic orbits are so unstable ($|\text{S.I.}| > 10$) that it is impossible to create the corresponding characteristic curve (see Fig. 3).

In the literature, there are some isolated examples of barred galaxy models, such as the "Cazes" bar (Barnes & Tohline 2001), the "model B" of Skokos et al. (2002b) and the "propeller" orbits in Kaufmann & Patsis (2005), all of which have the x_1 orbital family that is no longer the dominant one and other types of regular orbits play the leading role in supporting the barred structure. Thus, our simple galactic model can be considered as a member of this closed group. In our paper, we demonstrate that the role of x_1 orbits can be successfully supplemented by other types of regular families of orbits which can also support the bar. From a mathematical point of view, whether

an orbital family is present or not strongly depends on the choice of the potential describing the properties of the bar. The vast majority of papers devoted to the subject of barred galaxies utilize a Ferrers potential (Ferrers 1877) in order to model the bar. As it happens, the traditional x_1 orbital family dominates in galaxy models where a Ferrers potential is used. However, this does not necessarily mean that x_1 orbits should always dominate the structure of the phase plane of all 2D bar potentials used to model realistic galactic bars. In fact, in the present paper, we present evidence that numerous resonant orbits can also support the barred structure of a galaxy equally well.

4.1 Influence of the Strength of the Bar

To explore the influence of the strength of the bar α on the orbital structure of the barred galaxy, we let it vary while fixing the numerical values of all the other parameters in our model according to SM and integrate orbits for the set $\alpha = \{1, 2, 3, ..., 10\}$. Once the values of the parameters were chosen, we computed a set of initial conditions as described in Section 3 and integrated the corresponding orbits, computing the SALI of the orbits and then classifying the regular orbits into different families. Here we should point out that when $1.1 < \alpha < 2$ our model describes the properties of a weak rotating bar, but when $\alpha \geq 2$, we have the presence of a strong bar.

In Figure 5(a)–(f) we present six grids of initial conditions $(x_0, \dot{x_0})$ of orbits that we have classified for different values of the strength of the bar α. The numerical calculations reveal that when α varies there are eight main types of regular orbits. All the different regular families can be identified by the corresponding sets of islands which are formed in the phase plane. In particular, we see the eight main families already mentioned: (i) box orbits occupying the outer parts of the phase plane; (ii) 1:1 resonant orbits surrounding the two central main periodic point; (iii) 1:2 resonant orbits (type a) producing two stability islands; (iv) 1:3 resonant orbits generating three tiny islands at the outer parts of the grid; (v) 2:3 resonant orbits displaying a set of three islands; (vi) 3:4 resonant orbits forming a set of four islands; (vii) 3:5 resonant orbits producing a chain of five islands at the outer parts of the phase plane and (viii) 5:7 resonant orbits corresponding to a set of seven islands inside the box region. The term "other" refers to all different types of resonant orbits with $n, m < 9$ not included in the former categories. It is seen that apart from the several regions of regular motion, we observe the presence of a unified chaotic sea which surrounds all the islands of stability. The outermost black thick curve is the ZVC defined by Equation (8).

When $\alpha = 1$ the bar does not exist, the total potential is integrable and as expected there is no evidence whatsoever of chaotic motion in the phase plane of Figure 5(a). Almost the entire grid is covered by initial conditions corresponding to 1:1 resonant orbits, while we observe a thin layer of higher resonant 12:12 orbits (which is a bifurcation of the main 1:1 resonant family) at the prograde $(x > 0)$ side of the phase plane. The structure of the phase plane, however, changes drastically when $\alpha = 2$. We observe in Figure 5(b) that the area occupied by 1:1 orbits has been reduced and there are two distinct regions of stability; one at the right part of the grid corresponding to prograde 1:1 orbits and one at the left side corresponding to retrograde 1:1 orbits. We see, on the other hand, that box orbits swarm the outer parts of the grid, while several resonant families such as the cases of 2:3, 3:4, 4:5, 5:7 and 7:9 emerge inside the box area, thus producing sets of multiple stability islands. We also have to notice the presence of a small chaotic layer which defines the separation between 1:1 and box orbits. Things change even more as the strength of the bar increases. Figure 5(c) shows the structure of the phase plane when $\alpha = 4$, which corresponds to SM. It is evident that the chaotic layer has been transformed into a vast chaotic sea flooding the majority of the phase plane. The amount of box and higher resonant orbits has been reduced significantly and those orbits are confined to the outer parts of the grid. Two additional resonances, that is the 1:2 (type a) and the 3:5, emerge. When $\alpha = 4$ the potential of the bar is at integer resonance $1{:}\sqrt{\alpha}$=1:2, so we anticipated the existence of the 1:2 resonance. In Figure 5(d) where $\alpha = 6$, we observe that the extent of the chaotic sea has grown even further, mainly at the expense of box and 1:1 orbits. In fact, there are only a few isolated points in the grid corresponding to box orbits. On the contrary, the 1:2 stability islands have more than doubled their size.

Figure 5(e) and (f), where $\alpha = 8$ and $\alpha = 10$ respectively, indicates that a further increase in the strength of the bar has only a minor influence on the orbital structure of the phase plane. This is true because the amount of chaotic and 1:2 (type a) orbits seems to saturate. The most visible differences are the following: (i) the 1:1 prograde stability island disappears; (ii) box orbits gain ground again and (iii) some secondary resonances such as the 3:7 and 2:5 appear inside the box region. It should be noticed that the islands representing the 1:3 resonance are so small that they appear as isolated points in the grids of Figure 5(a)–(f).

Figure 6(a) shows the resulting percentages of chaotic orbits and those of the main families of regular orbits as α varies. It can be seen that there is a strong correlation between the percentages of most types of orbits and the value of the strength of the bar. When the bar is absent $(\alpha = 1)$, the entire phase plane is covered by 1:1 resonant orbits. As the strength of the bar is increased, however, the percentage of 1:1 resonant orbits decreases rapidly at an exponential rate. At the same time, the percentage of chaotic orbits increases and when $\alpha > 3$ chaotic orbits are the most populated family, always occupying more than 50% of the phase plane. In particular, the largest amount of chaos, around 75%, is observed when $\alpha = 5$. On the other hand, when $\alpha > 5$ the percentage of chaos is reduced almost linearly. The box orbits exhibit the peak of their percentage (around 40%) at $\alpha = 2$ and then for $2 < \alpha \leq 6$ their rate is reduced, while for $\alpha > 6$ this tendency is reversed. The

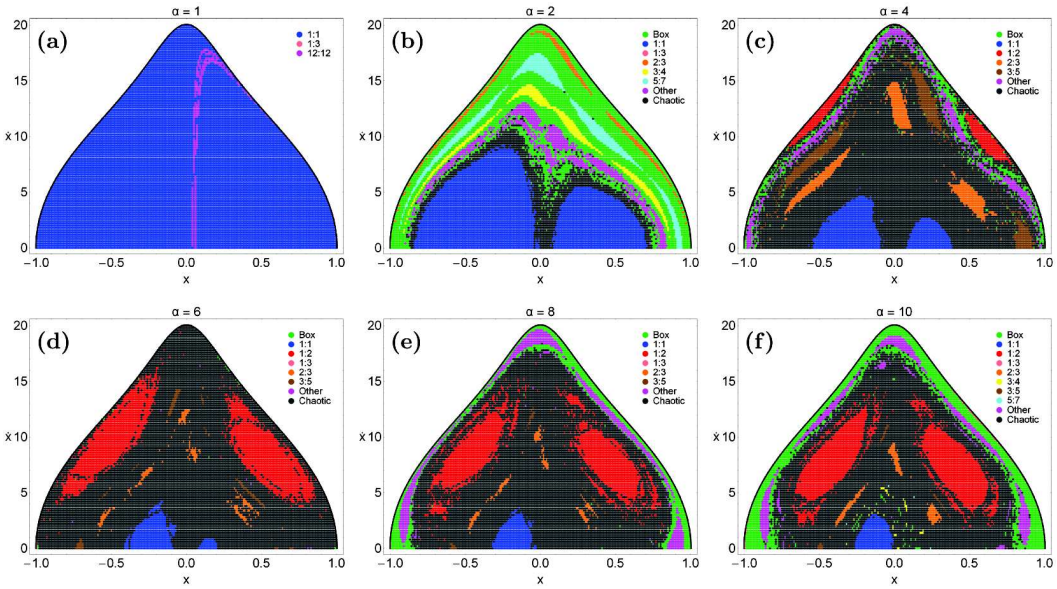

Fig. 5 Orbital structure of the $(x, \dot{x})$ phase plane of the barred galaxy model for different values of the strength of the bar α.

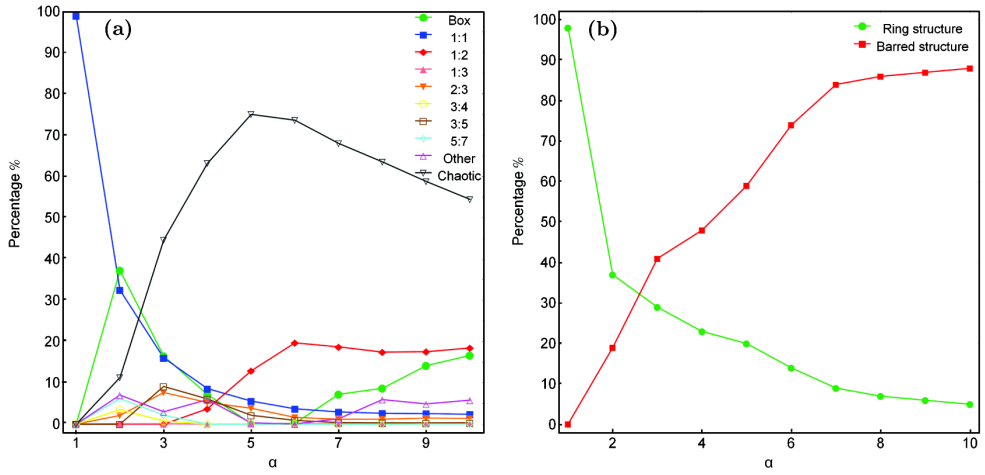

Fig. 6 Evolution of the percentages of (a-*left*): the different types of orbits in our barred galaxy model and (b-*right*): the types of regular orbits supporting the formation of nuclear rings or a barred structure, when varying the strength of the bar α.

percentage of the 1:2 resonant orbits starts to grow when $\alpha > 3$ and it seems to saturate around 20% when $\alpha > 6$. At higher values of the strength of the bar that are studied, the percentages of box and 1:2 resonant orbits (type a) tend to a common value (around 20%), thus sharing two-fifths of the entire phase plane. It is evident that in barred galaxies, varying the strength of the bar mainly shuffles the orbital content of all the other resonant orbits, whose percentages present fluctuations at low values (less than 10%). Thus, taking into account all the above, we could say that in barred galaxy models the strength of the bar α mostly influences box, 1:1, 1:2 (type a) and chaotic orbits. In fact, a large portion of 1:1 and box orbits turn into 1:2 (type a) and chaotic orbits as the bar becomes stronger, or in other words, as the value of α increases.

The evolution of the percentages of regular orbits supporting a ring or barred structure as a function of the strength of the bar α is shown in Figure 6(b). As we explained previously, we assume that only the 1:1 resonant orbits with $0.5 < g < 1.5$ support the formation of nuclear rings, while all types of regular orbits with $g \geq \sqrt{\alpha}$ support the barred structure. Here we have to point out that the percentages do not refer to the total number of tested orbits (regular plus chaotic) in each grid but rather to the total regular orbits. It is seen that for small values of α ($\alpha < 2.5$), as is the case of a weak bar, almost all the regu-

lar orbits favor the formation of nuclear rings. This is true because, as was discussed previously in Figure 5(a)–(b), the majority of the phase plane is covered by 1:1 regular orbits. However, as the value of α increases and the bar gains strength, the rate of 1:1 orbits which support rings decreases rapidly, while at the same time the percentage of regular orbits supporting a barred structure grows steadily and for $\alpha > 7$ it seems to saturate around 85%. Therefore, we may conclude that rings are highly favored in weak bar models, but in galaxy models possessing strong bars only roughly 5% of orbits support nuclear rings.

4.2 Influence of the Scale Length of the Nucleus

Our next step is to reveal how the overall orbital structure in our barred galaxy model is affected by the scale length of the nucleus $c_{\rm n}$. As usual, we let this quantity vary while fixing the values of all the other parameters according to SM and integrating orbits in the phase plane for the set $c_{\rm n} = \{0.05, 0.10, 0.15, ..., 0.50\}$. Our numerical calculations show that most of the main regular families are the same as in the previous case. The only difference is that in the group of regular families the 1:3 and 5:7 resonant families are now substituted by the 4:7 and 5:8 resonant families.

Figure 7(a)–(f) depicts six grids of initial conditions $(x_0, \dot{x_0})$ of orbits that we have classified for different values of the scale length of the nucleus $c_{\rm n}$. Again, all the different regular families can be identified by the corresponding sets of islands which are formed in the phase plane. It is observed in Figure 7(a) that when the central nucleus is very dense, that is when $c_{\rm n} = 0.05$, the vast majority of the phase plane is covered by chaotic orbits, but only the 1:1 resonant family survives. There is also weak evidence of the 2:3 resonance, however, the corresponding initial conditions are few and deeply buried in the vast chaotic sea. As we increase the value of $c_{\rm n}$ and consequently the central nucleus becomes less dense, we see in Figure 7(b) ($c_{\rm n} = 0.1$) and (c) ($c_{\rm n} = 0.2$) that additional regular families such as box, 1:2 (type a) and 3:5 emerge inside the chaotic sea. Moreover, the extent of the 1:1 and 1:2 stability islands grows as the scale length of the nucleus increases. The structure of the phase plane becomes very interesting in Figure 7(d) where $c_{\rm n} = 0.3$. This is true for many reasons. First of all, the amount of chaos is decreased and the prograde 1:1 stability island disappears. At the outer parts of the phase plane, box orbits take control, but the 1:2 stability islands are significantly reduced. It can also be seen that the entire phase plane is swarmed by many types of resonant orbits producing several sets of stability islands. In particular, the 2:3 and 3:5 are the most populated resonant families.

In Figure 7(e) and (f) we present the cases where $c_{\rm n} = 0.4$ and $c_{\rm n} = 0.5$ respectively, that is when the central nucleus is sparse enough. In both cases, the structure of the grid is similar and we observe that the entire phase plane is only covered by regular orbits. In fact, a large portion of the grid corresponds to box orbits, but all the resonant families exist inside the box region. We should notice that the 1:2 resonance is completely absent when the scale length of the spherical nucleus obtains high values. Furthermore, the 1:1 stability island is now located almost at the center of the grid, thus containing a mixture of prograde and retrograde 1:1 orbits. It should also be pointed out that as the central nucleus becomes more dense (small values of $c_{\rm n}$) there is an increase in the allowed velocity $\dot{x}$ of the stars near the center of the galaxy.

The resulting percentages of chaotic and regular orbits for the barred galaxy model as the scale length of the nucleus $c_{\rm n}$ varies are shown in Figure 8(a). It is evident that box and chaotic orbits are the types of orbits mainly affected by the scale length of the nucleus. In particular, we see that when the central nucleus is very dense ($c_{\rm n} < 0.15$) the motion of stars is highly chaotic since about 90% of the entire phase plane is covered by chaotic orbits. However, as the values of $c_{\rm n}$ increase and the nucleus becomes less dense ($c_{\rm n} > 0.2$), the percentage of chaos displays a sharp decrease and eventually vanishes when $c_{\rm n} > 0.35$. The rate of box orbits, on the other hand, only starts to grow when the nucleus is sparse enough ($c_{\rm n} > 0.2$) and when $c_{\rm n} > 0.3$ box orbits are the dominant type occupying about two-thirds of the phase plane. It can be seen in Figure 8(a) that all the other types of resonant orbits are considerably less affected by the shifting of $c_{\rm n}$. The rate of 1:1 resonant orbits exhibits minor fluctuations for small values of the scale length, however, when $c_{\rm n} > 0.3$ it increases, while at the same time the percentage of the 1:2 (type a) resonant orbits vanishes. The evolution of the percentages of the 2:3, 3:5 and higher resonant families of orbits exhibit a similar pattern; they start to grow when $c_{\rm n} > 0.15$ and they decrease for $c_{\rm n} > 0.35$. The percentages of the 4:7 and 5:8 resonant families on the other hand, only have nonzero values when $c_{\rm n} > 0.25$ and then it seems they saturate around 2%. Therefore, increasing the scale length of the nucleus (in other words the nucleus becomes less concentrated and dense) in barred galaxy models turns mainly chaotic orbits into box orbits, while resonant orbits are less affected.

Figure 8(b) shows the evolution of the percentages of regular orbits supporting a ring or barred structure[3] as a function of the scale length of the nucleus $c_{\rm n}$. We observe that when the central nucleus is dense enough the vast majority of regular orbits support nuclear rings, however, as the nucleus becomes less dense the rate of regular orbits that support the bar grows constantly and when $c_{\rm n} > 0.25$ it dominates. At the same time, the percentage of ring structure orbits decreases rapidly and saturates around 20% when $c_{\rm n} > 0.3$. Thus, one may conclude that in barred galaxy models with dense nuclei only the formation of nuclear rings is favored, but when the central nucleus is sparse enough about 40% of the total types of

[3] According to SM $\alpha = 4$, thus the threshold value for the ratio g is $\sqrt{\alpha} = 2$.

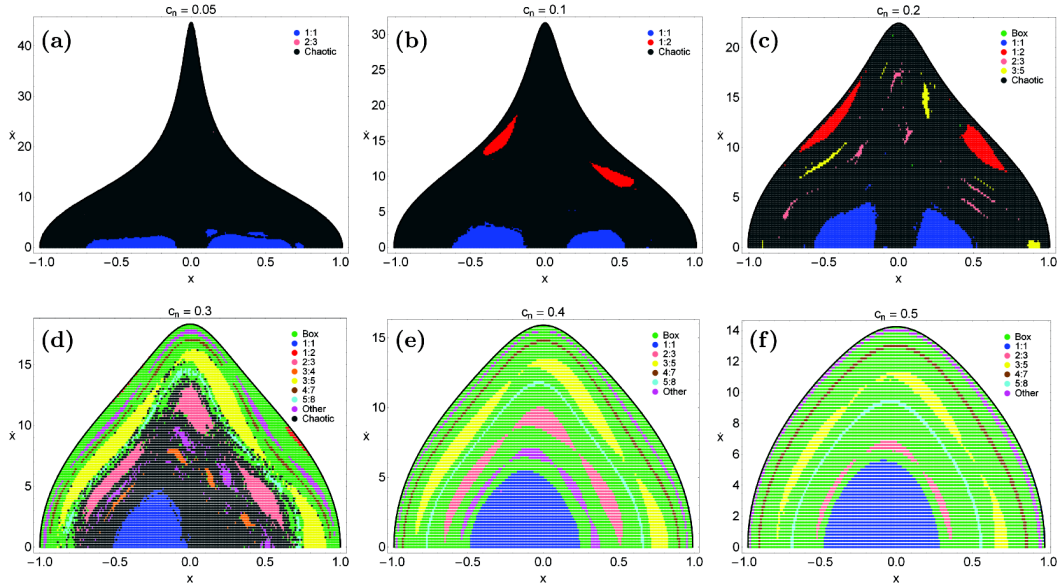

Fig. 7 Orbital structure of the $(x, \dot{x})$ phase plane of the barred galaxy model for different values of the scale length $c_{\rm n}$ of the central spherical nucleus.

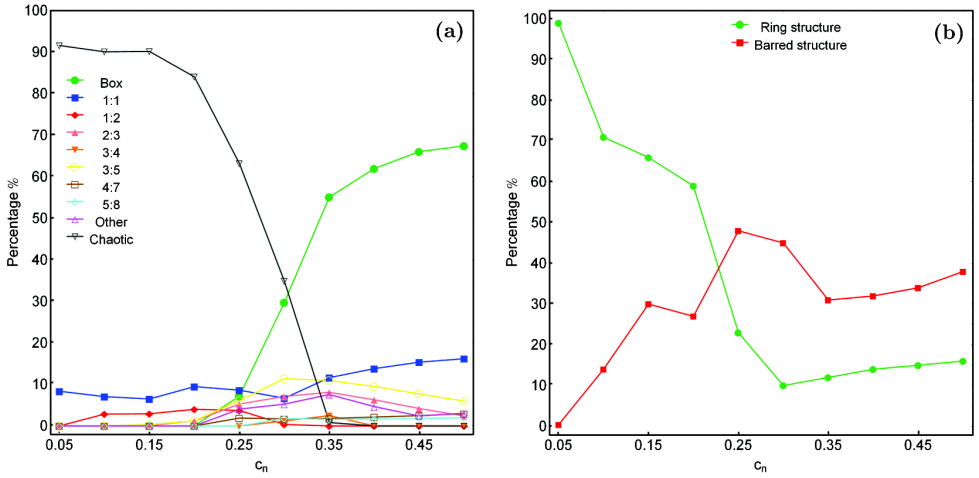

Fig. 8 Evolution of the percentages of (a-*left*): the different types of orbits in our barred galaxy model and (b-*right*): the types of regular orbits supporting the formation of nuclear rings or a barred structure, when varying the scale length $c_{\rm n}$ of the central spherical nucleus.

regular orbits support the barred structure and only 20% of them support nuclear rings.

4.3 Influence of the Angular Velocity

The next parameter under investigation is the angular velocity $\Omega_{\rm b}$ of the bar. We shall try to understand how the overall orbital structure in our barred galaxy model is influenced by this parameter. Again, we let this quantity vary while fixing the values of all the other parameters of our galactic model according to SM and integrating orbits in the phase plane for the set $\Omega_{\rm b} = \{0, 0.25, 0.5, ..., 2.5\}$. The numerical experiments indicate that in this case, the main families of regular orbits are similar to those discussed in subsection 4.2.

In order to explore the structure of the phase plane when $\Omega_{\rm b}$ varies, we integrated orbits in several grids. A sample of six grids of initial conditions $(x_0, \dot{x}_0)$ of orbits that we have classified for different values of the angular velocity is given in Figure 9(a)–(f). As usual, all the different types of regular families can be easily identified by the corresponding sets of islands which are produced in the phase plane. In Figure 9(a) we present the case where $\Omega_{\rm b} = 0$ which means that the bar does not rotate. Due to the absence of rotation, the Coriolis force is zero and therefore, the phase plane is symmetrical with respect to the $x = 0$ axis. We observe a unified chaotic domain at the central parts of the phase plane, but there are also numerous stability islands corresponding to resonant families.

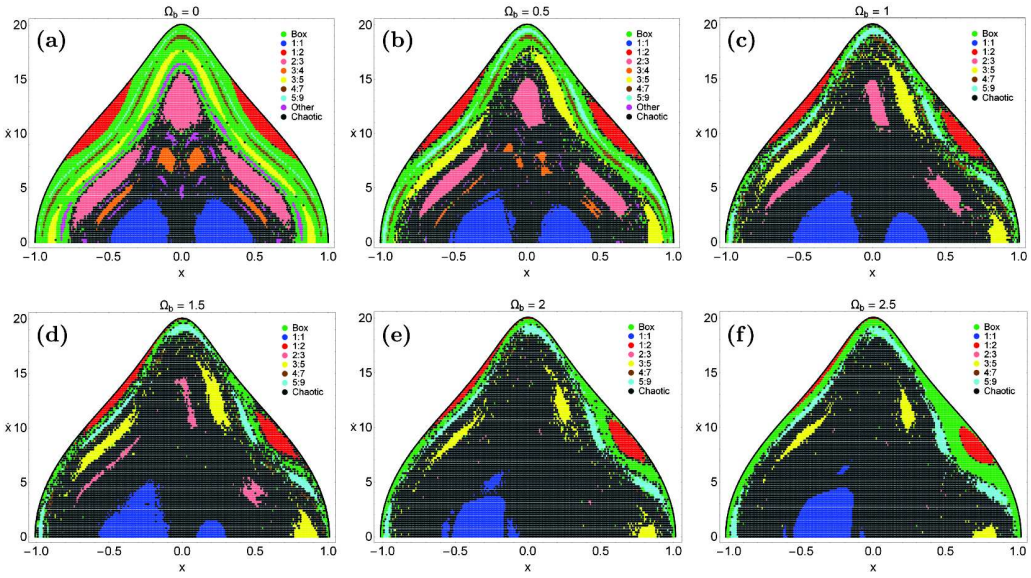

Fig. 9 Orbital structure of the $(x, \dot{x})$ phase plane of the barred galaxy model for different values of the angular velocity $\Omega_{\rm b}$ of the bar.

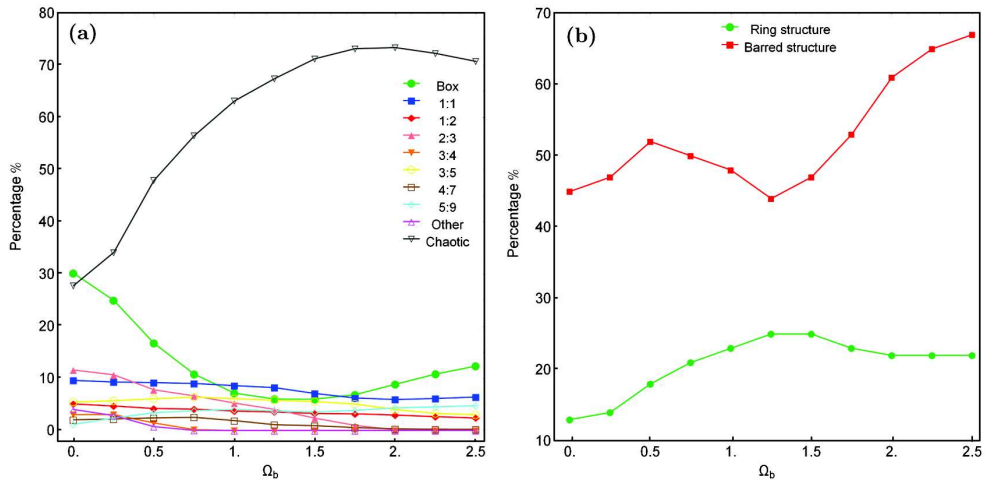

Fig. 10 Evolution of the percentages of (a-*left*): the different types of orbits in our barred galaxy model and (b-*right*): the types of regular orbits supporting the formation of nuclear rings or a barred structure, when varying the angular velocity of the bar $\Omega_{\rm b}$.

When $\Omega_{\rm b} = 0.5$, which is a model of a slowly rotating bar, it can be seen in Figure 9(b) that the structure of the phase displays minor differences with respect to Figure 9(a), with the growth of the region occupied by chaotic orbits and the depopulation of box, 2:3, 3:4 and higher resonant orbits being most visible. As the bar gains speed, this tendency is continued in Figure 9(c) ($\Omega_{\rm b} = 1$) and (d) ($\Omega_{\rm b} = 1.5$) and as a result the 3:4 and higher resonant orbits are completely absent. In Figure 9e where $\Omega_{\rm b} = 2$, we see that the prograde 1:1 stability island disappears, while the 2:3 resonance has been depopulated so much that the corresponding initial conditions appear as isolated points in the grid. The region of box orbits, on the other hand, seems to increase. It is evident from Figure 9(f), that in the case of a fast rotating bar ($\Omega_{\rm b} = 2.5$), the region of box orbits increases even further, thus suppressing the 1:2 (type a) stability islands. One may reasonably conclude that the faster the rotation of the bar is, the more chaos is observed in the barred galaxy.

Figure 10(a) shows the evolution of the resulting percentages of chaotic and regular orbits for the barred galaxy model as the angular velocity $\Omega_{\rm b}$ varies. Once more we see that the angular velocity mainly affects the fraction of box and chaotic orbits. When there is no rotation of the bar ($\Omega_{\rm b} = 0$), box and chaotic orbits seem to share about 60% of the phase plane. As the value of the angular velocity increases and the bar gains speed, we observe that the percentages of both box and chaotic orbits evolve similarly but with different directions. Being more precise, the rate of box orbits decreases until $\Omega_{\rm b} = 1.25$, but for

larger values of the angular velocity it exhibits an increase. The percentage of chaotic orbits, on the other hand, increases rapidly, however, when $\Omega_{\rm b} > 1.75$ it displays a minor decrease. Nevertheless, the motion of stars is highly chaotic throughout as the percentage of chaotic orbits remains larger than any other individual regular family. In fact, in most cases more than half of the phase plane is occupied by chaotic orbits and the peak (around 75%) is observed when $\Omega_{\rm b} = 1.75$. One may see in Figure 10(a) that all the other types of resonant orbits are considerably less affected by the shifting of $\Omega_{\rm b}$. The rate of the 1:1 resonant orbits decreases, especially for $\Omega_{\rm b} > 1.25$ when the prograde 1:1 stability islands starts to shrink until it disappears completely from the phase plane. In the same vein, the percentage of the 1:2 resonant (type a) family exhibits a minor almost linear decrease. The rate of the 2:3 family, on the contrary, shows a rapid reduction and vanishes when $\Omega_{\rm b} > 2$. The 3:4 and higher resonant orbits seem to be unable to cope with the rotation of the bar and their rates are zeroed very quickly even at low speed ($\Omega_{\rm b} > 0.75$). Here we should point out that only the 5:9 resonant family is favored by the rotation of the bar since it is the only regular family that constantly augments its rate with increasing $\Omega_{\rm b}$. Therefore, increasing the angular velocity of the bar generally turns different types of regular orbits into chaotic ones.

The evolution of the percentages of regular orbits supporting either a ring or barred structure as a function of the angular velocity of the bar $\Omega_{\rm b}$ is given in Figure 10(b). We observe that the majority of regular orbits support the barred structure throughout, but only about one-fifth of the total regular orbits support the formation of nuclear rings. In particular, for relatively small speeds ($\Omega_{\rm b} < 1.25$) the rate of ring structure orbits increases, reaching about 25%, while for larger values of the angular velocity it saturates around 20% of the total regular orbits. At the same time, the rate of regular orbits supporting a barred structure displays a small fluctuation around 45% and only in models with fast rotating bars ($\Omega_{\rm b} > 1.25$) increases rapidly, occupying more than two-thirds of regular orbits. Therefore, we may conclude that slowly rotating bars support the formation of nuclear rings, but fast rotating bars mainly favor the barred structure.

4.4 Influence of the Energy

The last parameter under investigation is the total orbital energy $E_{\rm J}$. In order to explore how the energy level affects the overall orbital structure of our barred galaxy model, we use the normal procedure according to which we let the energy vary while fixing the values of all the other parameters of our galactic models according to SM. At this point, we should point out that the particular value of the energy determines the maximum possible value of the x coordinate ($x_{\max}$) on the $(x, \dot{x})$ phase plane. To select the energy levels, we chose those values of the energy which give $x_{\max} = \{0.5, 1, 1.5, ..., 4\}$. Our numerical computations show that the main families of regular orbits remain the same as those discussed in the previous two subsections.

Figure 11(a)–(f) shows six grids of initial conditions $(x_0, \dot{x_0})$ of orbits that we have classified for different values of the Jacobi integral $E_{\rm J}$. In Figure 11(a), $E_{\rm J} = -77$ which corresponds to local motion of stars moving very close to the central nucleus with $x_{\max} = 0.5$ kpc. It is seen that the vast majority of the phase plane is covered by initial conditions of regular orbits, while a weak chaotic layer exists at the central parts of the grid separating regions of box and 1:1 resonant orbits. We also observe the presence of several chains of stability islands inside the box region. These sets of stability islands are produced by secondary resonances such as the 4:5, 5:6, 5:7, 6:7 and 7:9 families. The grid shown in Figure 11(b) where $E_{\rm J} = 1$ is very similar to those discussed earlier in Figures 5(c) and 9(c). Figure 11(c) shows a grid where $E_{\rm J} = 80$ and $x_{\max} = 1.5$ kpc. Here the area occupied by chaotic orbits is reduced, as there is a considerable increase of the 1:2 (type a) stability islands. The increase in the amount of 1:2 (type a) resonant orbits continues in Figure 11(d) where $E_{\rm J} = 290$. In this case, box and 1:2 resonant orbits (type a) share the majority of the phase plane. A weak chaotic layer is, however, still present, but the 1:1 resonance is confined to the center of the grid producing multiple stability islands. The 1:2 resonance takes over almost the entire phase plane in Figure 11(e) where $E_{\rm J} = 593$. In this case we should note that apart from the 1:2 type resonance, the 1:2 type b (corresponding to figure-eight orbits) emerges at the outer parts of the phase plane. Things are quite different in Figure 11(f) where $E_{\rm J} = 780$ and $x_{\max} = 4$ kpc. We see a small decrease in the extent of the 1:2 (type a) islands due to the increase in the amount of box orbits at the outer parts of the phase plane, while 1:2 type b orbits disappear. At the center of the grid we can distinguish a well-formed 1:1 stability island, while in the neighborhood there is a mixture of delocalized initial conditions corresponding to chaotic, 1:1 and higher resonant orbits.

Looking at Figure 11(a)–(f) we see that, as the value of the energy increases, in other words we study the motion of stars moving at larger distances from the galactic center, the 1:2 resonant orbits dominate the vast majority of the phase plane. Here we should notice that according to SM the value of the strength of the bar is $\alpha = 4$, so the potential of the harmonic oscillator used for the description of the bar is at resonance; the 1:2 resonance to be more precise. Thus, a natural and fair question arises: what happens to the phase plane if we change the value of the strength of the bar? To give an answer to this question, we chose the value $\alpha = 9$ (which also corresponds to integer resonance; 1:3) and reconstructed the grid of initial conditions shown in Figure 11(e). Our results are given in Figure 12. Now, the harmonic oscillator is at the 1:3 resonance and it can be seen that the 1:3 resonance prevails, while the 1:2 resonant orbits define two small stability islands confined to the center of the grid. This is because the model assumes

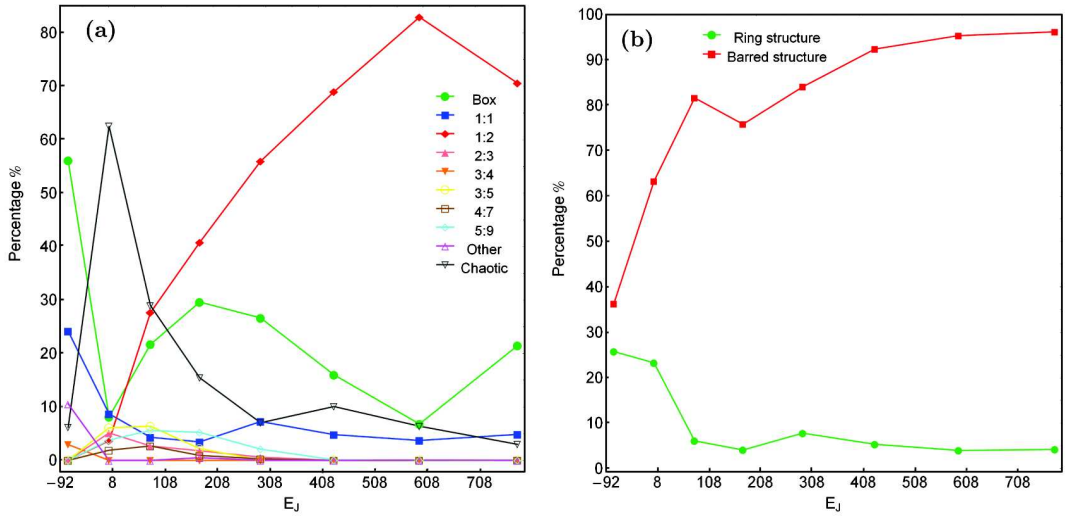

Fig. 11 Orbital structure of the $(x, \dot{x})$ phase plane of the barred galaxy model for different values of the Jacobi integral $E_{\rm J}$.

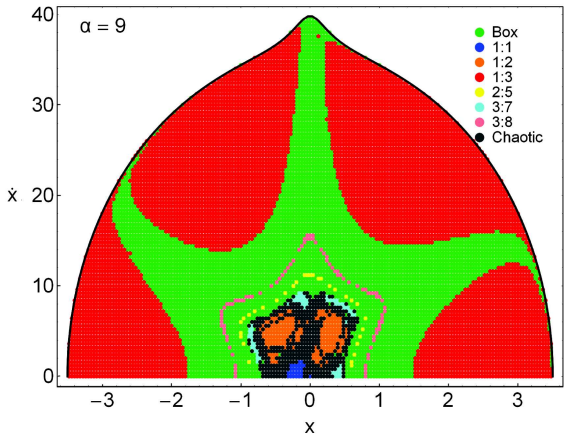

Fig. 12 Orbital structure of the $(x, \dot{x})$ phase plane of the barred galaxy model when $\alpha = 9$ and $E_{\rm J} = 593$, while the values of all the other parameters are defined according to SM. We observe that the 1:3 resonant orbits occupy the vast majority of the phase plane.

a constant ratio of x and y frequencies throughout, which however generally is not the case. Therefore, we conclude that for high values of the orbital energy corresponding to star orbits moving sufficiently far from the central nucleus ($x_{\max} > 1.5$ kpc), the influence of the bar prevails over that of the central nucleus.

In the following Figure 13(a) we present the evolution of the resulting percentages of chaotic and regular orbits for the barred galaxy model as the value of the energy $E_{\rm J}$ varies. We observe that when the motion of stars is at low energies, i.e., orbits which move very close to the galactic center, they are highly regular, with box and 1:1 resonant orbits being the most populated families. The largest amount of chaotic orbits (around 65%) is observed when the value of energy is near zero, but with increasing $E_{\rm J}$ their rate drops rapidly and at higher energy values it eventually vanishes. The percentage of box orbits displays strong fluctuations with sudden drops and peaks. The rate of the 1:1 resonant orbits on the other hand, for $E_{\rm J} > 55$, evolves almost monotonically, keeping a constant value around 5%. It is also seen that the percentage of 1:2 (type a) resonant orbits starts to grow sharply as soon as the energy grows and when $E_{\rm J} > 100$ the 1:2 (type a) family is the dominant type. In fact, we see that for high values of the Jacobi integral ($E_{\rm J} = 600$) the 1:2 resonant orbits take over more than 80% of the entire phase plane, although for larger values of energy their rates exhibit a small decrease due to the simultaneous increase of the box orbits. All the other resonant families seem to be immune to the increase in energy since their percentages are almost unperturbed throughout; all these families practically disappear when $E_{\rm J} > 400$. Taking into consider-

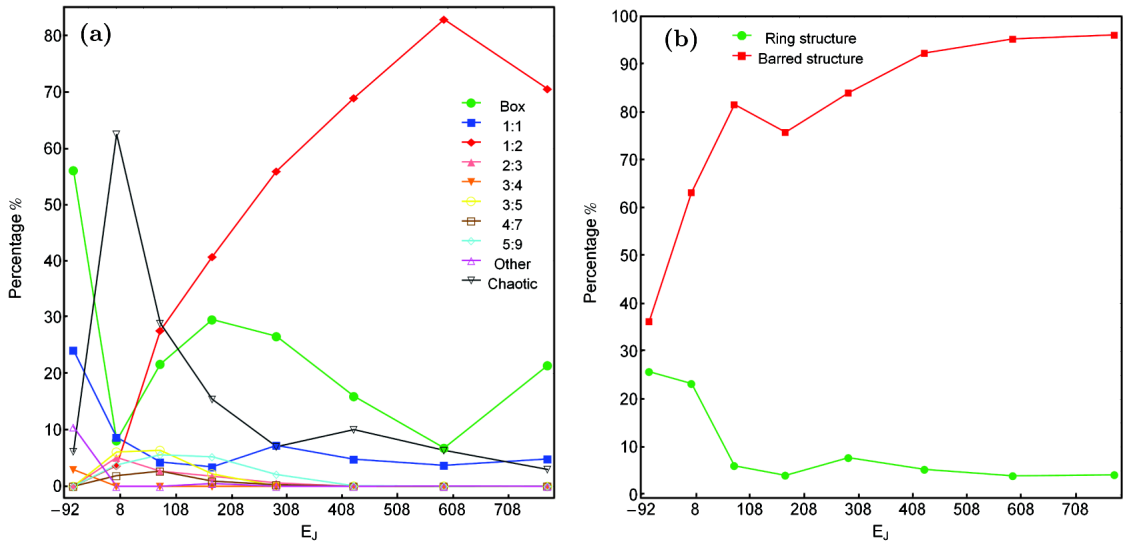

Fig. 13 Evolution of the percentages of (a-*left*): the different types of orbits in our barred galaxy model and (b-*right*): the types of regular orbits supporting the formation of nuclear rings or a barred structure, when varying the value of the Jacobi integral $E_{\rm J}$.

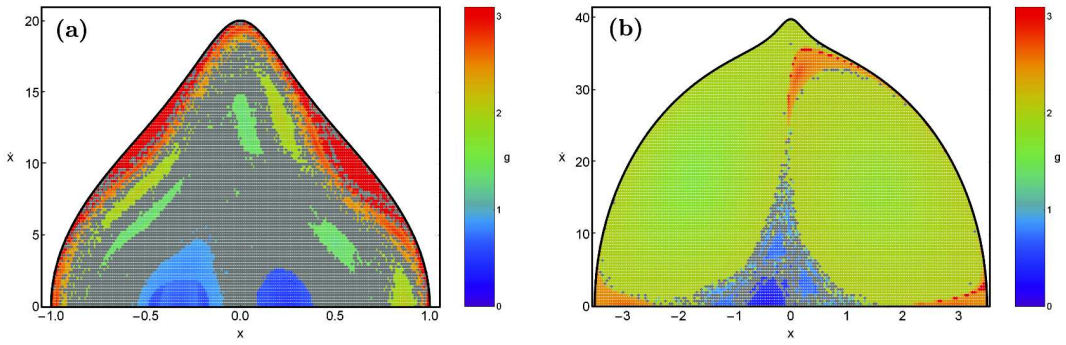

Fig. 14 Grids of initial conditions $(x_0, \dot{x_0})$ when (a-*left*): $E_{\rm J} = 1$ and (b-*right*): $E_{\rm J} = 593$. Each point is colored according to the value of the ratio g, thus distinguishing between regular orbits supporting ring formation $(0.5 < g < 1.5)$ and a barred structure $(g \geq 2)$.

ation all the above-mentioned analysis, we may conclude that in barred galaxy models the value of energy mostly affects the chaotic, box, 1:1 and 1:2 (type a) resonant orbits. We would like to point out that the 1:2 type b resonant orbits are only present in barred galaxy models with high enough energy.

Of particular interest is to interpret the evolution of the percentages of regular orbits supporting a ring or barred structure as a function of the Jacobi integral $E_{\rm J}$. Our numerical results are given in Figure 13(b) where it can be seen that the barred structure is always more favored. To be more precise, for low energies ($E_{\rm J} < 20$) only about 25% of the total regular orbits support the formation of nuclear rings, while for larger values of energy the rate drops to around 5% and remains there throughout. On the contrary, we see that the percentage of regular orbits supporting the bar grows rapidly with increasing energy, although in high energy models ($E_{\rm J} > 410$) their percentage seems to saturate around 90%. Summarizing, low energy models support the formation of both nuclear rings and bars, while high energy models are only favored for barred structures.

Figure 14(a)–(b) shows another perspective related to the grids of Figure 11(b) and (e). Here, each initial condition is colored according to the value of the ratio g, thus distinguishing between regular orbits supporting ring formation $(0.5 < g < 1.5)$ and a barred structure $(g \geq 2)$. It becomes evident that the 1:1 resonant orbits indeed support the formation of nuclear rings, while the 1:2 (type a and b) resonant orbits support the barred structure of the galaxy.

5 CONCLUSIONS

In this work, we used an analytic galactic gravitational model which embraces the general features of a barred galaxy containing a spherical, dense and massive nucleus. The choice of the model potential for the description of the bar was made mainly taking into account the fact that near the center of a galaxy the motion of stars can be approximated by harmonic oscillations. Our aim was to investigate how the basic parameters of the Hamiltonian system influence the level of chaos and also the distribution of regular families in our barred galaxy model. Our results strongly suggest that both the level of chaos and the distribution of regular families are indeed very dependent on the parameters of the galaxy. We believe that the presented outcomes can provide interesting information regarding the structure and properties of barred galaxies.

In our research, we chose to investigate the influence of four basic quantities that are part of the galactic model, namely the strength of the bar, the scale length of the nucleus, the angular velocity of the bar and the value of the total orbital energy (Jacobi constant). We decided not to explore the influence of the mass of the nucleus for two main reasons: (i) it has been extensively studied in earlier works (see, e.g. Hasan & Norman 1990; Hasan et al. 1993; Zotos 2012a; Zotos & Carpintero 2013) and (ii) in this model the mass of the nucleus significantly affects the size of the grid (in other words the values of $x_{\max}$ and $\dot{x_{\max}}$), so it was impossible to set a constant energy level and then vary the mass of the nucleus. We also tried to find out which regular orbits support the barred structure of the galaxy and which support the formation of nuclear rings, using the g value as the only criterion for this task. The main results of our research can be summarized as follows:

(1) Perhaps the most important finding of our research is the fact that the traditional x_1 orbital family does not always dominate the structures of all 2D barred galaxy models, thus verifying similar outcomes (see, e.g. Barnes & Tohline 2001; Skokos et al. 2002b; Kaufmann & Patsis 2005). Indeed, we have presented numerical evidence that several resonant orbits which are not related to the x_1 family can support the bar.
(2) In our barred galaxy model, several types of regular orbits exist, but there are also extended chaotic domains separating the areas of regularity. In particular, a large variety of resonant orbits (i.e. 1:1, 1:2, 1:3, 2:3, 3:4, 3:5, 4:7, 5:7, 5:8, 5:9 and higher resonant orbits) are present, thus making the orbital structure richer. Here we must clarify that by the term "higher resonant orbits" we refer to resonant orbits with a rational quotient of frequencies made from integers > 5, which of course do not belong to the main families.
(3) It was found that in barred galaxy models the strength of the bar α mostly influences box, 1:1, 1:2 and chaotic orbits, turning a large portion of 1:1 and box orbits into 1:2 and chaotic orbits as the bar becomes stronger, or in other words, as the value of α increases. As expected, galaxy models with relatively strong bars do not favor the formation of nuclear rings.
(4) Increasing the scale length of the nucleus (in other words the nucleus becomes less concentrated and dense) mainly turns chaotic orbits into box orbits, while resonant orbits are less affected. Dense nuclei only favor the formation of nuclear rings, but when the central nucleus is sparse enough about 40% of the total types of regular orbits support the barred structure and only 20% of them the nuclear rings.
(5) As the bar gains speed, different types of regular orbits become chaotic, occupying more than 70% of the entire phase plane. We found that slowly rotating bars support the formation of nuclear rings, while fast rotating bars mainly favor the barred structure.
(6) A strong correlation between the value of the energy and the percentages of chaotic, box, 1:1 and 1:2 resonant orbits was found to exist. Moreover, low energy models support the formation of both nuclear rings and bars, while high energy models only favor the barred structure.

We consider the present results as an initial effort and also a promising step in the task of understanding the orbital structure of barred galaxies. Taking into account that our outcomes are encouraging, it is in our future plans to utilize a logarithmic potential for describing the properties of the bar, thus expanding our investigation in global motion as well as into three dimensions, exploring how the basic parameters influence the nature of the 3D orbits. Furthermore, of particular interest would be to reveal the complete network of periodic orbits, thus shedding some light on the evolution of periodic orbits as well as their stability when varying all the available parameters of the galactic model.

Acknowledgements The authors would like to express their warmest thanks to the anonymous referee for the careful reading of the manuscript and for all the apt suggestions and comments which allowed us to significantly improve both the quality and the clarity of our paper.

Appendix A: STICKY ORBITS AND NUMERICAL INTEGRATION TIME

Usually, when investigating the regular or chaotic nature of orbits in galactic potentials, we try to keep the integration time as long as 1 Hubble time because this allows us to relate the calculations to our Universe. However, in previous research (Zotos & Carpintero 2013; Zotos & Caranicolas 2014) we demonstrated that when using short integration time intervals (equal to about 1 to 10 Hubble times), a non-negligible number of chaotic orbits were misclassified as regular by several chaos indicators. This phenomenon is also true in the present case.

Figure A.1 shows, for the set of orbits in the SM model, how the number of regular orbits shifted along with

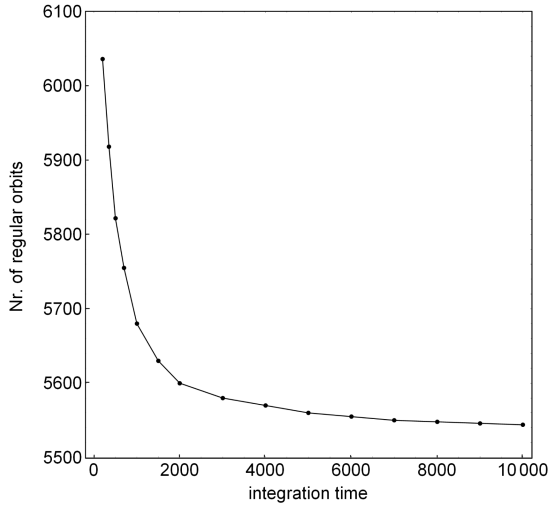

Fig. A.1 Evolution of the total number of orbits classified as regular in the SM model, using the SALI chaos indicator, as a function of the total time of the numerical integration. The threshold value of SALI was fixed at 10^{-7}.

the time span of the orbital integration. As a reference, Table A.1 shows, for each of the models that was studied in Section 4, the total number of orbits identified as chaotic at 10^2 and also at 10^4 time units of numerical integration. It is evident from Table A.1, that when using integration time much longer than 1 Hubble time, the number of misclassified orbits in every model has been considerably reduced (the maximum relative error that was measured was about 7%). Nevertheless, even this extended numerical integration does not completely solve the problem; in fact, there will always be (in a non integrable potential) sticky orbits which behave as regular ones during arbitrarily large times, rendering any attempt to develop an algorithm which finds them all in a short time hopeless.

Table A.1 Total number of orbits identified as chaotic at 10^2 (N) and at 10^4 (N') time units of numerical integration for all studied models.

α	$c_{\rm n}$	$\Omega_{\rm b}$	$E_{\rm J}$	N	N'	Error (%)
1	0.25	1	1.5	0	0	0
2	0.25	1	1.5	1575	1651	4.6
3	0.25	1	1.5	6459	6749	4.3
4	0.25	1	1.5	8971	9463	5.2
5	0.25	1	1.5	10498	11253	6.7
6	0.25	1	1.5	10506	11106	5.4
7	0.25	1	1.5	9972	10207	2.3
8	0.25	1	1.5	5363	5592	4.1
9	0.25	1	1.5	8409	8851	5.0
10	0.25	1	1.5	7628	8108	5.9
4	0.05	1	1.5	12905	13802	6.5
4	0.10	1	1.5	12997	13511	3.8
4	0.15	1	1.5	12822	13509	5.1
4	0.20	1	1.5	12027	12607	4.6
4	0.25	1	1.5	8971	9463	5.2
4	0.30	1	1.5	5083	5256	3.3
4	0.35	1	1.5	146	148	1.5
4	0.40	1	1.5	0	0	0
4	0.45	1	1.5	0	0	0
4	0.50	1	1.5	0	0	0
4	0.25	0.00	1.5	4123	4203	1.9
4	0.25	0.25	1.5	5072	5108	0.7
4	0.25	0.50	1.5	6949	7201	3.5
4	0.25	0.75	1.5	8358	8556	2.3
4	0.25	1.00	1.5	8971	9463	5.2
4	0.25	1.25	1.5	9785	10056	2.7
4	0.25	1.50	1.5	10062	10648	5.5
4	0.25	1.75	1.5	10295	10952	6.0
4	0.25	2.00	1.5	10502	10950	4.1
4	0.25	2.25	1.5	10412	10812	3.7
4	0.25	2.50	1.5	10039	10657	5.8
4	0.25	1	–77	918	931	1.4
4	0.25	1	1	8866	9452	6.2
4	0.25	1	80	4152	4351	4.6
4	0.25	1	174	2339	2392	2.2
4	0.25	1	290	1014	1055	3.9
4	0.25	1	430	1495	1512	1.1
4	0.25	1	593	976	972	2.8
4	0.25	1	780	451	455	0.9

References

Athanassoula, E. 1984, Phys. Rep., 114, 319

Athanassoula, E. 1992, MNRAS, 259, 345

Athanassoula, E., Bienayme, O., Martinet, L., & Pfenniger, D. 1983, A&A, 127, 349

Barnes, E. I., & Tohline, J. E. 2001, ApJ, 551, 80

Benedict, G. F., Howell, D. A., Jørgensen, I., Kenney, J. D. P., & Smith, B. J. 2002, AJ, 123, 1411

Binney, J., & Spergel, D. 1982, ApJ, 252, 308

Binney, J., & Spergel, D. 1984, MNRAS, 206, 159

Binney, J., & Tremaine, S. 2008, Galactic Dynamics: Second Edition (Princeton: Princeton Univ. Press)

Bountis, T., Manos, T., & Antonopoulos, C. 2012, Celestial Mechanics and Dynamical Astronomy, 113, 63

Buta, R., Treuthardt, P. M., Byrd, G. G., & Crocker, D. A. 2000, AJ, 120, 1289

Caranicolas, N., & Barbanis, B. 1982, A&A, 114, 360

Caranicolas, N. D. 1998, A&A, 332, 88

Caranicolas, N. D., & Karanis, G. I. 1998, Ap&SS, 259, 45

Caranicolas, N. D., & Papadopoulos, N. J. 2005, Baltic Astronomy, 14, 535

Caranicolas, N. D., & Papadopoulos, N. J. 2007, Astronomische Nachrichten, 328, 556

Caranicolas, N. D., & Zotos, E. E. 2010, New Astron., 15, 427

Caranicolas, N. D., & Zotos, E. E. 2013, PASA, 30, 49

Carpintero, D. D., & Aguilar, L. A. 1998, MNRAS, 298, 1

Carpintero, D. D., & Muzzio, J. C. 2012, Celestial Mechanics and Dynamical Astronomy, 112, 107

Combes, F., Debbasch, F., Friedli, D., & Pfenniger, D. 1990, A&A, 233, 82

Comerón, S., Knapen, J. H., Beckman, J. E., et al. 2010, MNRAS, 402, 2462

Contopoulos, G., & Barbanis, B. 1985, A&A, 153, 44

Contopoulos, G., & Grosbol, P. 1989, A&A Rev., 1, 261

Contopoulos, G., & Magnenat, P. 1985, Celestial Mechanics, 37, 387

Contopoulos, G., & Mertzanides, C. 1977, A&A, 61, 477

Contopoulos, G., & Papayannopoulos, T. 1980, A&A, 92, 33

Englmaier, P., & Gerhard, O. 1997, MNRAS, 287, 57
Eskridge, P. B., Frogel, J. A., Pogge, R. W., et al. 2000, AJ, 119, 536
Ferrers, N. M. 1877, The Quarterly Journal of Pure and Applied Mathematics, 14, 1
Friedli, D., & Martinet, L. 1993, A&A, 277, 27
Hasan, H., & Norman, C. 1990, ApJ, 361, 69
Hasan, H., Pfenniger, D., & Norman, C. 1993, ApJ, 409, 91
Hsieh, P.-Y., Matsushita, S., Liu, G., et al. 2011, ApJ, 736, 129
Kaufmann, D. E., & Contopoulos, G. 1996, A&A, 309, 381
Kaufmann, D. E., & Patsis, P. A. 2005, ApJ, 624, 693
Kim, W.-T., Seo, W.-Y., & Kim, Y. 2012a, ApJ, 758, 14
Kim, W.-T., Seo, W.-Y., Stone, J. M., Yoon, D., & Teuben, P. J. 2012b, ApJ, 747, 60
Knapen, J. H., Beckman, J. E., Heller, C. H., Shlosman, I., & de Jong, R. S. 1995, ApJ, 454, 623
Knapen, J. H. 2004, in Astrophysics and Space Science Library, 319, Penetrating Bars Through Masks of Cosmic Dust, ed. D. L. Block, I. Puerari, K. C. Freeman, R. Groess, & E. K. Block, 189
Kormendy, J., & Kennicutt, Jr., R. C. 2004, ARA&A, 42, 603
Lees, J. F., & Schwarzschild, M. 1992, ApJ, 384, 491
Maciejewski, W., Teuben, P. J., Sparke, L. S., & Stone, J. M. 2002, MNRAS, 329, 502
Manos, T., & Athanassoula, E. 2011, MNRAS, 415, 629
Manos, T., Bountis, T., & Skokos, C. 2013, Journal of Physics A Mathematical General, 46, 254017
Marinova, I., & Jogee, S. 2007, ApJ, 659, 1176
Mazzuca, L. M., Knapen, J. H., Veilleux, S., & Regan, M. W. 2008, ApJS, 174, 337
Muñoz-Tuñón, C., Caon, N., & Aguerri, J. A. L. 2004, AJ, 127, 58
Muzzio, J. C., Carpintero, D. D., & Wachlin, F. C. 2005, Celestial Mechanics and Dynamical Astronomy, 91, 173
Olle, M., & Pfenniger, D. 1998, A&A, 334, 829
Pfenniger, D. 1984, A&A, 134, 373
Pfenniger, D. 1996, in Astronomical Society of the Pacific Conference Series, 91, IAU Colloq. 157: Barred Galaxies, ed. R. Buta, D. A. Crocker, & B. G. Elmegreen, 273
Pichardo, B., Martos, M., & Moreno, E. 2004, ApJ, 609, 144
Piner, B. G., Stone, J. M., & Teuben, P. J. 1995, ApJ, 449, 508
Press, W. H., Teukolsky, S. A., Vetterling, W. T., & Flannery, B. P. 1992, Numerical Pecipes in FORTRAN. The Art of Scientific Computing (Cambridge: Cambridge Univ. Press)
Regan, M. W., & Teuben, P. 2003, ApJ, 582, 723
Sandstrom, K., Krause, O., Linz, H., et al. 2010, A&A, 518, L59
Sellwood, J. A., & Wilkinson, A. 1993, Reports on Progress in Physics, 56, 173
Sheth, K., Regan, M. W., Scoville, N. Z., & Strubbe, L. E. 2003, ApJ, 592, L13
Sheth, K., Vogel, S. N., Regan, M. W., Thornley, M. D., & Teuben, P. J. 2005, ApJ, 632, 217
Skokos, C. 2001, Journal of Physics A Mathematical General, 34, 10029
Skokos, C., Patsis, P. A., & Athanassoula, E. 2002a, MNRAS, 333, 847
Skokos, C., Patsis, P. A., & Athanassoula, E. 2002b, MNRAS, 333, 861
Thakur, P., Ann, H. B., & Jiang, I.-G. 2009, ApJ, 693, 586
Šidlichovský, M., & Nesvorný, D. 1996, Celestial Mechanics and Dynamical Astronomy, 65, 137
Zotos, E. E. 2011, Baltic Astronomy, 20, 339
Zotos, E. E. 2012a, New Astron., 17, 576
Zotos, E. E. 2012b, Nonlinear Dynamics, 69, 2041
Zotos, E. E. 2013, Nonlinear Dynamics, 73, 931
Zotos, E. E., & Caranicolas, N. D. 2013, A&A, 560, A110
Zotos, E. E., & Caranicolas, N. D. 2014, Nonlinear Dynamics, 76, 323
Zotos, E. E., & Carpintero, D. D. 2013, Celestial Mechanics and Dynamical Astronomy, 116, 417